Fluid Ablation Interactions on a Compression Ramp at Mach 8

Başkaya, A.O.; Hickel, S.; Dungan, Sean ; Brehm, Christoph

DOI
10.2514/6.2024-0501

Publication date
2024

Document Version
Final published version

Published in
Proceedings of the AIAA SCITECH 2024 Forum

AIAA SciTech Forum
8-12 January 2024, Orlando, FL
AIAA SCITECH 2024 Forum

10.2514/6.2024-0501

Fluid-Ablation Interactions on a Compression Ramp at Mach 8

Ata Onur Başkaya[1]* and Stefan Hickel [1]†
[1]*Delft University of Technology, 2629HT Delft, The Netherlands*

Sean Dungan[2]‡ and Christoph Brehm[2]§
[2]*University of Maryland, College Park, MD, 20742, USA*

Direct numerical simulations (DNS) are performed over a 15° compression ramp undergoing ablation at Mach 8 to examine fluid-ablation interactions (FAI) on transitional high-speed boundary layers. The experiments at these conditions with a rigid wall are first numerically replicated for a laminar flow. Heating streaks are introduced by introducing perturbations in the baseflow informed by prior stability calculations. The ramp is then replaced by a low-temperature ablator in our DNS and the interaction of the streaks with the recessing ablator surface are examined. Different approaches from two independently developed solvers are used to study this problem. Overall, both solvers provide qualitatively and quantitatively very similar results; however, differences in streak amplification and mass blowing magnitudes are observed. We discuss the difficulties in accurately predicting ablation and present the first findings regarding its influence on the perturbation evolution and transition to turbulence for this configuration.

I. Introduction

Vehicles traveling at hypersonic speeds must operate in extreme flight environments. Severe mechanical and thermal loads are the primary concern for aerothermodynamists, who seek to ensure the survival of the onboard payload. In addition to strategic shaping of the outer mold line, ablative surface materials have been and continue to be deployed as an effective means for redirecting heat away from the payload. When exposed to the high heating and temperatures of the surrounding flow field, the ablative surface material will typically first undergo endothermic chemical reactions with the surrounding fluid medium. Subsequently, the ablative material will then be blown away from the surface and into the boundary layer formed around the body. These two mechanisms of surface reactions and blowing rarely occur in a spatially uniform manner and even less so when the surrounding flow is transitioning from a laminar to a turbulent state. The turbulent flow enhances heat transfer and consequently the ablation rate. Larger heat and mass transfer results in rapid evolution of the shape, constructing a feedback cycle, which persists throughout the high-temperature flight duration. Such phenomenon in this flow regime are critical since delaying or promoting earlier transition holds important implications for the thermal and mechanical loads imposed on the vehicle.

Accurate simulations of atmospheric entry flows require research in many diverse fields of study. Pieces of this highly multi-disciplinary problem has been tackled from different fronts by many research groups over the last six decades. Review articles on this past research have been compiled for studying laminar to turbulent transition [1–4] with roughness [5] as well as with ablation [6, 7]. As for more recent studies from the past few years, notable contributions have been made in modeling GSI [8–10], performing laminar hypersonic simulations with ablation coupling [11–13], investigating stability and transition to turbulence in hypersonic flows [14–19] with roughness [20, 21] or with blowing [22, 23] and further with ablation [24–28], and in performing turbulent hypersonic simulations [29, 30]. Moreover, there has also been a recently renewed interest for studying ablative shape change with low-temperature ablators [13, 31, 32] as they exhibit characteristics similar to that of real flight ablators at lower enthalpy conditions. There still exists large uncertainties in the predictions and interactions of various effects, and some phenomena such as transition control with roughness [20] is yet to be understood properly. Among all of these studies, use of direct numerical simulations (DNS) has been greatly influential in many of the aforementioned works due to the lack of reliable

*Ph.D. Candidate, Aerospace Engineering, High Speed Aerodynamics Lab, A.O.Baskaya@tudelft.nl; Student Member AIAA
†Full Professor, Aerospace Engineering, High Speed Aerodynamics Lab; S.Hickel@tudelft.nl; Member AIAA
‡Graduate Research Assistant, Aerospace Engineering, 3179 Glenn L. Martin Hall Bldg; sdungan@umd.edu; Student Member AIAA
§Associate Professor, Aerospace Engineering, 3179 Glenn L. Martin Hall Bldg; cbrehm1@umd.edu; Member AIAA

data in this field as ground testing cannot simultaneously replicate all aspects of atmospheric entry environments, and flight tests are rare.

Fluid-ablation interactions (FAI) are technically a coupled problem between fluid and solid dynamics, though, and more work is needed to investigate how important the ablation coupling is between the transitional boundary layer and material response. Three recent works have made strides in this direction. Trevino [33] in 2021 implemented a camphor subliming boundary condition with implicit time integration into US3D [34] to perform DNS of fluid-ablation interactions. Their solver was able to generate the progression of smooth surfaces to narrow grooves at moderate Reynolds numbers. A factor 10^4 acceleration was applied to the recession rates that didn't impact the surface mass or energy balance but was used to observe significant topological changes within the simulated fluid time. Patel [35] in 2023 did something similar in his investigation of camphor ablation in the presence of a transitional flow over a backward-facing step. The separation of time scales was handled by artificially speeding up ablation rates by considering the Damkhöler number defined as $Da_w = u_2/v_w$, or the ratio of post-shock velocity to wall velocity. Moving boundary ablation simulations showed considerable generation of vorticity over the camphor surface, however, ablation affecting specific boundary layer instability modes was not an objective of that research and, therefore, was not investigated. The same year, Dungan et al. [36] investigated camphor FAI over a straight cone at Mach 5.3. Using a loose coupling approach with curvilinear meshes and one-dimensional ray material response solvers, the authors showed only minor destabilization of first mode disturbances due to ablation. However, it was shown that significant fluid-solid coupling between the heat transfer and recession distributions is possible. In light of all this, much work remains to exact the FAI effect on high-speed transitional boundary layers, as well as the most effective means to numerically simulate the problem.

This works seeks to make progress in this direction by studying FAI for Mach 8 transitional flow over a 15° compression ramp. Experiments performed using identical geometry and flow conditions exhibited significant heat transfer streaks at reattachment [37]. Numerical work by Dwivedi et al. [38] showed the separated flow selectively amplifies steady Görtler-like vortices that possess a spanwise wavelength similar to those observed in the experiments. Thus, this case should serve as a good proxy for studying FAI in the presence of realistic surface roughness and blowing.

After numerically replicating the experimental conditions, the rigid ramp will be replaced by solid camphor to study the ablation of this low-temperature ablator. Two separate numerical frameworks (CHAMPS and INCA) will be used as a means of validation and exploration of slightly different techniques for solving the same problem. This manuscript is organized as follows: Section II enumerates the governing equations for the problem at hand and presents the physical modeling approaches, Section III presents the 2-D base flow solutions to compare agreement in fundamental flow quantities, then Section IV considers the 3-D compression ramp under perturbed flow conditions to produce steady streaks, which interact with the ramp undergoing ablative recession. Conclusive remarks are made in Section V.

II. Governing Equations and modeling

The compressible Navier-Stokes equations for a multispecies chemically-inert fluid can be written as

$$\frac{\partial \mathbf{U}}{\partial t} + \boldsymbol{\nabla} \cdot \mathbf{F}(\mathbf{U}) = 0\,, \tag{1}$$

where $\mathbf{U} = [\rho_i, \rho u, \rho v, \rho w, \rho E]^{\mathrm{T}}$ is the vector of conserved variables, and $\mathbf{F} = \mathbf{F}_{inv} + \mathbf{F}_{vis}$ is the sum of inviscid and viscous fluxes. Along the x axis, they take the following forms:

$$\mathbf{F}_{inv} = \begin{bmatrix} \rho_i u \\ \rho u^2 + p \\ \rho u v \\ \rho u w \\ u(\rho E + p) \end{bmatrix}, \quad \mathbf{F}_{vis} = \begin{bmatrix} J_{\mathrm{x},i} \\ -\tau_{\mathrm{xx}} \\ -\tau_{\mathrm{xy}} \\ -\tau_{\mathrm{xz}} \\ -(\tau_{\mathrm{xx}} u + \tau_{\mathrm{xy}} v + \tau_{\mathrm{xz}} w) + q_{\mathrm{x}} \end{bmatrix}, \tag{2}$$

where ρ_i is the species partial density for the i^{th} species, $\mathbf{u}$ is the mixture average velocity, ρ is the mixture density, p is the mixture pressure, and $E = e + u^2/2$ is the specific total energy, which is the sum of the thermodynamic internal energy e and the kinetic energy. Note that the species source term is taken as zero as no homogeneous gas-phase reactions are occurring at the conditions studied in this work. Heterogeneous reactions due to ablation govern the species concentrations and approaches taken to model them are discussed in Section II.B. modeling approaches for the species diffusion flux $\mathbf{J}_i$, the viscous stress tensor $\boldsymbol{\tau}$, and the total heat flux $\mathbf{q}$ are mentioned in Section II.A.

In the absence of ablation, single species air is used as the fluid in this work. Gas viscosity is modeled by Sutherlands's law, specific heats are taken to be constant, and thermal conductivity is obtained from a Prandtl number of 0.72. When camphor is introduced as a species, cubic polynomials for viscosity and thermal conductivity presented by Zibitsker et al. [39] are employed with a unit Prandtl number. For diffusion, Lewis number is taken as unity.

A. Numerical Methods

Two independently developed solvers are considered in this work. INCA is a high-fidelity finite-volume solver for direct numerical simulations (DNS) and large eddy simulations (LES) of the compressible chemically reacting Navier-Stokes equations and provides a large number of different discretization schemes on three-dimensional block-Cartesian AMR grids [40, 41]. For the purposes of this study, a third-order weighted essentially non-oscillatory (WENO) scheme [42] with HLLC flux function [43] is selected to discretize the inviscid terms. Second-order centered differences are used for the viscous terms and the explicit third-order Runge-Kutta scheme of Gottlieb and Shu [44] is selected for time integration. The ablating wall is represented by a cut-element IB method [45], which is a consistent and conservative extension of the finite-volume flux balance, in INCA. This approach accurately accounts for cells being split by boundaries by considering the cut-elements that form from the intersection of the Cartesian grid and the surface geometry triangulation. Details of this method and its extension to catalytic and ablative immersed boundaries have been presented by Başkaya et al. [46, 47].

The second solver used in this work is the CHAMPS framework being developed at the University of Maryland. Similar to INCA, the computational domain is divided up into a Cartesian, block-structured mesh, which supports adaptive mesh refinement (AMR). Regular fluid cells (ones for which their differentiation stencil does not touch a solid boundary) compute inviscid fluxes using a Rusanov flux function and were reconstructed using a fifth-order WENO scheme[48]. The viscous fluxes were computed using a second-order accurate centered scheme. More special care is required when fluid cells have stencils that include cells inside the geometry (irregular cells). This is handled with a locally-stabilized finite difference stencil detailed in Ref. 49. Simulations without ablation were obtained with backward differentiation formula (BDF1) implicit time integration, but once ablation was included a strong-stability preserving Runge-Kutta 4-stage, 3rd-order explicit time integration scheme was used. Note, the body-fitted (BF) suite inside CHAMPS was utilized for the 2D baseflow calculations.

B. Fluid-Ablation Interaction

Both INCA and CHAMPS solvers employ different methodologies to incorporate fluid-ablation interactions. INCA considers a gas-surface interaction (GSI) boundary condition, while CHAMPS is coupled with a material response (MR) solver. Both the GSI [46, 47] and MR [39] methods have been described and successfully demonstrated in several reference works. Here, only the differences within the approaches are discussed.

The GSI approach operates as a dedicated boundary condition for the cut-element IB method of INCA, which makes use of the subroutines provided by the Mutation^{++} library [50]. Assuming steady-state inside the material, this approach does not require or provide information inside the interior of the solid material. For this study, only a mass balance is considered and the ramp wall is assumed to be isothermal at 293 K. Details of this GSI approach are presented by Başkaya et al. [47].

The MR method used inside CHAMPS was developed by Zibitzker et al. [51] and coupled into CHAMPS by McQuaid et al. [52–55]. It discretizes the surface geometry into individual one-dimensional rays of camphor and solves a transient heat conduction problem with a contracting grid scheme for each one. In addition to the mass balance equations solved by INCA's GSI boundary condition, CHAMPS MR framework also solves a momentum and an energy balance at the surface to consider variable blowing and temperatures along the ramp wall.

Both methods essentially solve for the mass blowing rate $\dot{m} = \sum_i \dot{\omega}_{i,wall}$, calculated as the sum of the species source term $\dot{\omega}_{i,wall}$. The speed at which ablation products blow out of the surface is calculated by

$$v_{blow} = \frac{\dot{m}}{\sum_i \rho_i} \, . \tag{3}$$

Values obtained for species densities and mass blowing speeds are imposed as boundary conditions for the Navier-Stokes equations. Similarly, the speed at which the surface recesses is given by

$$v_{wall} = \frac{\dot{m}}{\rho_s} \, , \tag{4}$$

where ρ_s is the solid density. The recession speeds are used to evolve the surface geometry over time according to the coupling approaches of the two solvers.

III. 2-D Compression Ramp: Base Flow Analysis

We first consider a 2-D compression ramp to establish the base flow for the 3-D case, which will be discussed in Section IV. Results obtained with INCA and CHAMPS are compared to assess how well the predictions from these independently-developed solvers agree. Following a comparison with an inert isothermal wall, an ablative boundary condition is imposed on the ramp to compare the predictions of mass blowing rates.

A. Geometry and Flow Conditions

The geometry under consideration here is a 15° compression ramp, which is shown schematically in Fig. 1. The computational setup numerically replicates the experiments of Chuvakhov et al. [37]. A flat plate with a sharp leading edge of length $L = 0.05$ m is followed by a ramp inclined 15° with respect to the horizontal (i.e., flow direction) of length $2L$. Only a portion of the geometry near the corner is shown in Fig. 1 for $x \in [0, 0.1]$ m to better highlight the separation region straddling the compression corner at $x = 0.05$ m. The freestream conditions are listed in Table 1. The reported Reynolds number based on length (Re_L) might be more readily contextualized by reporting it per unit length, or $Re = 7.4(10^6)$/m. Single-species air is considered with inert isothermal wall boundary conditions over the leading edge and the ramp.

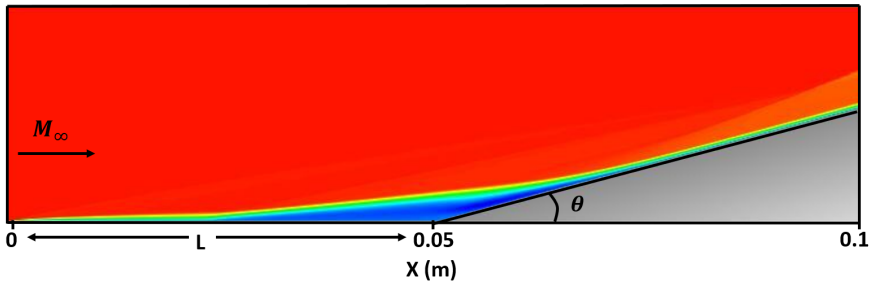

Fig. 1 Base flow and geometry for 2-D compression ramp.

Table 1 Freestream conditions for the considered compression ramp.

M_∞	P_∞ (Pa)	T_∞ (K)	T_{wall} (K)	$Re_L(10^5)$
8	355	55	293	3.7

B. Base Flow Results

The steady, laminar solution to Eq. 1 for the given freestream conditions is computed using both the IB method of the INCA solver and the body-fited method of the CHAMPS solver. Mach number and pressure fields presented in Figs. 2 and 3 showcase good agreement between the solvers as both solvers successfully predict the Mach wave emanating from the leading edge and the pressure jump downstream of the reattachment shock. Similarly, temperature contours in Fig. 4 indicate a good qualitative agreement for the recirculation region and the peak temperatures predicted beyond the reattachment shock by both solvers.

For a more quantitative comparison, the skin friction coefficient

$$C_f = \frac{\tau_w}{\frac{1}{2}\rho_\infty U_\infty^2} \tag{5}$$

with τ_w as the shear stress, and the Stanton number

$$St = \frac{q_w}{\rho_\infty U_\infty c_p (T_r - T_w)}. \tag{6}$$

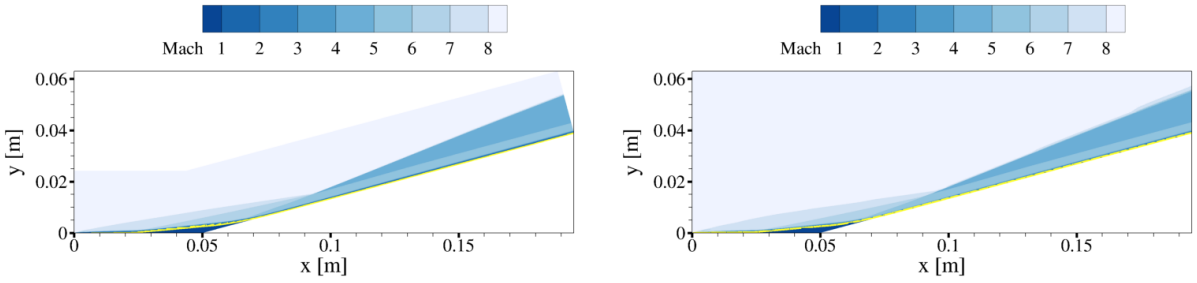

Fig. 2 Comparison of Mach number contours with (a) the BF method of CHAMPS and (b) the IB method of INCA for the 2-D base flow. The bright line indicates the sonic line.

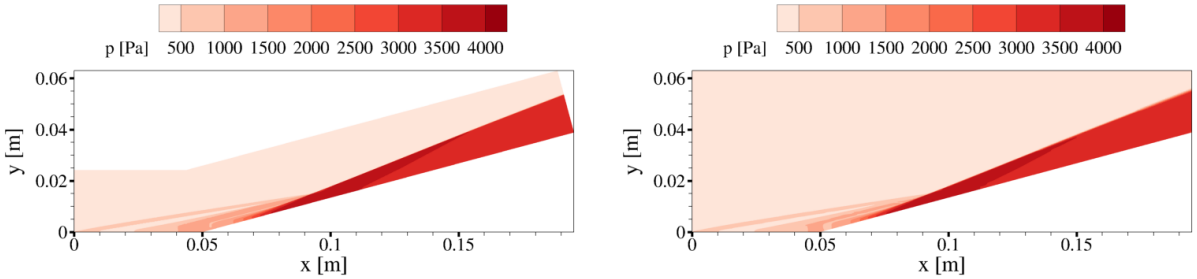

Fig. 3 Comparison of pressure contours with (a) the BF method of CHAMPS and (b) the IB method of INCA for the 2-D base flow. The bright line indicates the sonic line.

are calculated along the wall. A recovery factor of 0.0846 was used in the calculation of the recovery temperature T_r. The specific heat at constant pressure is taken as $c_p = 1005$ J/(kg·K). Good agreement between the solvers for both of these quantities is presented in Fig. 5. The Stanton numbers are additionally compared with the results of Dwivedi et al. [38]. Slight variations arise in the vicinity of peak heat transfer, where the detached shock impinges on the ramp. This is attributed to the differences in the numerical schemes between the solvers and the grid topologies leading to different resolutions in capturing the reattaching shock. Skin friction coefficients on the other hand show an excellent agreement between INCA and CHAMPS.

C. Base Flow with Ablative Blowing

The inert isothermal wall boundary condition on the ramp is replaced with an ablative boundary condition to compare the predicted mass blowing rates by the two solvers. The surface material of the ramp is assumed to be made of solid camphor and only the sublimation reaction

$$C_{10}H_{16}O_{(solid)} \rightarrow C_{10}H_{16}O_{(gas)} \,, \tag{7}$$

is considered. Vapor pressure and material properties for the Air-Camphor mixture is taken to be as in the work of Rotondi et al. [13].

Steady mass blowing rates predicted by both solvers are compared in Fig. 6. Qualitatively the blowing rates are similar although it was noticed that INCA is predicting a higher mass blowing rates than CHAMPS. This disagreement in the results is believed to be due to several differences in the fluid-ablation interaction models of the two solvers. We have seen that the additional energy balance solved by the CHAMPS solver only predicts a variation on the order of 0.1 K, which should not cause this variation. Another major difference is that CHAMPS calculates the species diffusion velocities at the surface by a modified Fick's law, whereas INCA calculates them through a detailed Stefan-Maxwell diffusion model. Regardless, both solvers qualitatively predict very similar profiles. Hence, we expect that the physical

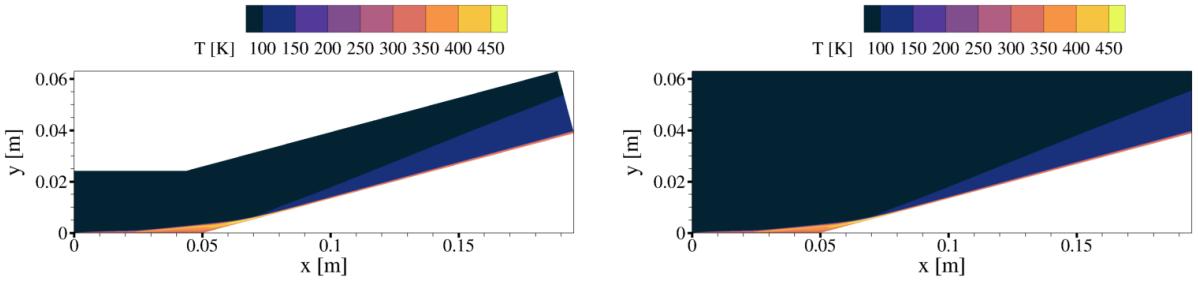

(a) **(b)**

Fig. 4 Comparison of temperature contours with (a) the BF method of CHAMPS and (b) the IB method of INCA for the 2-D base flow.

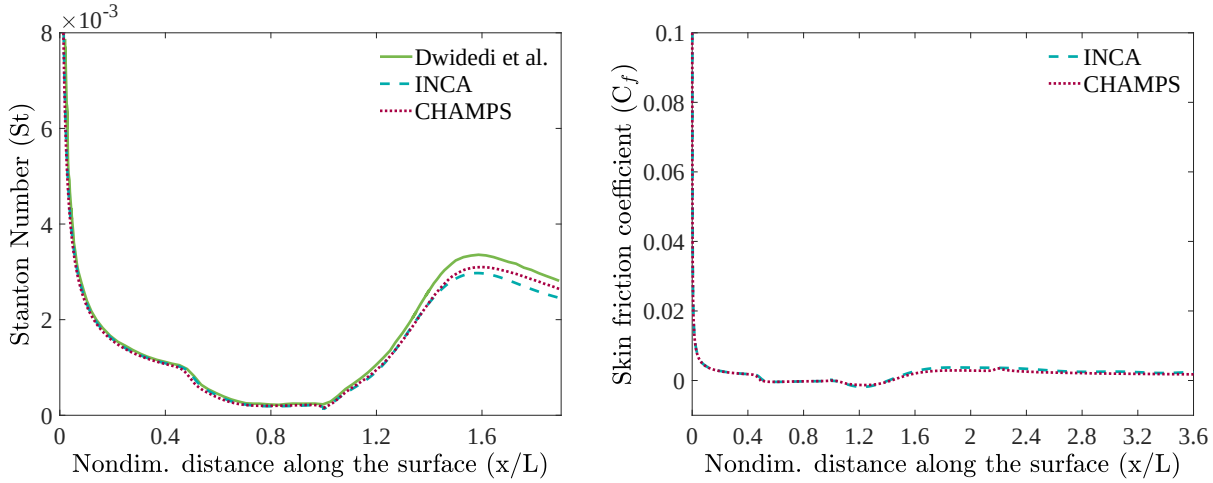

(a) **(b)**

Fig. 5 Comparison of (a) skin friction coefficients and (b) Stanton numbers along the surface of the 2-D compression ramp.

modeling approaches are sensitive to the same quantities, and that the results of each of the approaches will yield similar solutions. Only difference would be that the ablative response to the flow would be of a different magnitude.

D. Linear Stability

The time spectral solver in the CHAMPS frame work was utilized as an inexpensive precursor calculation to ensure the 2D baseflow obtained would support the instabilities to be studied in the 3D framework with ablation. This solver, developed by Haas et al. [56], solves directly for the time-spanwise periodic disturbance state for a given frequency spanwise-wavenumber pair when small perturbations are introduced into the domain. The disturbance was introduced through a volume source term limited to a small region upstream of the separation bubble. The small-amplitude forcing of the spatial form listed in [57] and with near zero temporal frequency (essentially steady) generates a steady streak that undergoes very large amplification near the location where the boundary layer reattaches on the inclined ramp (i.e., reattachment). This can be seen visually by the contours of disturbance x-direction velocity and temperature (u' and T') in Fig 7a and Fig 7b, respectively. The higher disturbance amplitude (yellow) in both figures dominates the contour colors right around $x = 0.065$. This amplification was quantified more by extracting wall-normal profiles and computing the maximum in disturbance kinetic energy and temperature for each profile. The progression of these quantities is shown in Fig 8a and Fig 8b. Plotted on the log scale, one can see that disturbance kinetic energy is amplified by roughly 6 order of magnitude from the separation to the end of the computational domain. Maximum in disturbance temperature

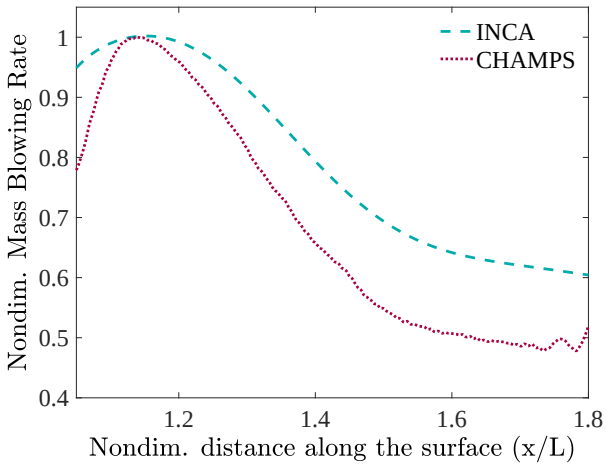

Fig. 6 Comparison of normalized mass blowing rates along the surface of the 2-D compression ramp.

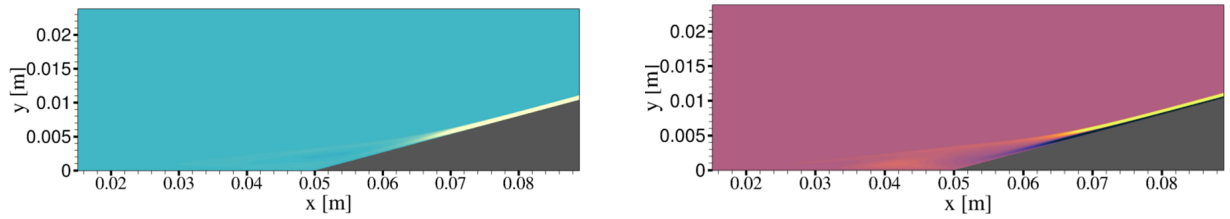

Fig. 7 Disturbance in (a) streamwise velocity and (b) temperature fields obtained with the time spectral solver.

along each wall-normal profile also undergoes large amplification by roughly 5 orders of magnitude. These results agree qualitatively with those of Dwivedi et al. [38]. With these results in hand, it was clear the baseflows obtained would support the desired disturbance growth the 3D studies sought to investigate.

IV. 3-D Compression Ramp: Fluid-Ablation Analysis on Perturbed Flow

Following the agreement in the results of the 2-D base flows in Section III, the solutions with the inert isothermal wall are extruded in the spanwise direction by 0.003 m to obtain the 3-D base flows. The flow is then perturbed according to the chosen forcing function to obtain steady streaks over the ramp. Then, the rigid ramp is numerically replaced by a solid camphor ramp, allowing it to undergo ablative recession. This section investigates how the variation in the temperature and the mass fraction distributions due to the steady streaks influences the ablation over the solid camphor ramp. For computational efficiency, streamwise domain is truncated at 0.1 m for most the 3-D simulations. Results with an extended domain up to 0.2 m are presented in Section IV.B.2 to investigate perturbation growth.

A. Perturbed Flow with Steady Streaks

Following the stability analysis in Section III.D, both solvers proceeded to perturb the flow by a forcing function with wavelength $\lambda = 0.003$ m active along the entire spanwise domain and from $x = 0.02$ m to $x = 0.023$ m in the streamwise direction. The resulting steady streaks are shown through slices at $x = [0.023, 0.030, 0.070]$ m in Fig. 9. These figures indicate two counter rotating vortices in the streamwise direction, forming a steady streak. It can be seen that the numerical predictions of both solvers are in very good agreement.

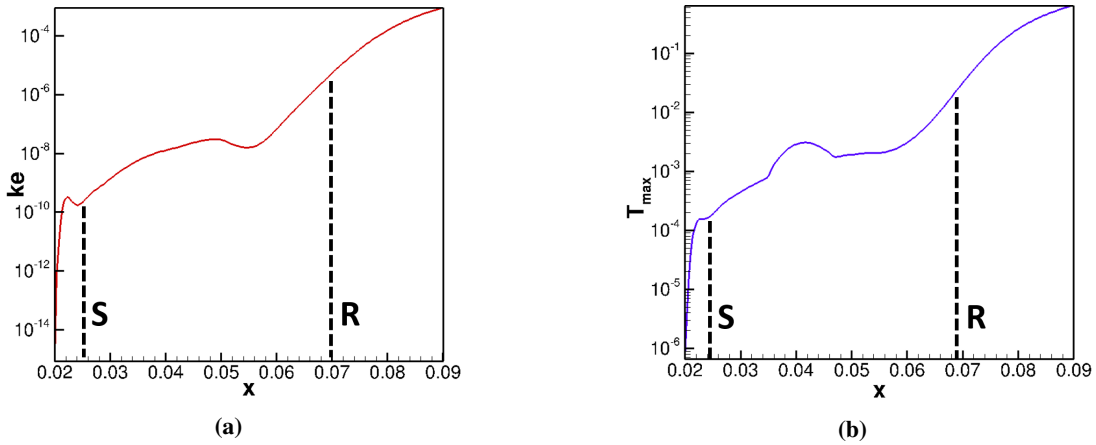

Fig. 8 Wall-normal maximum in disturbance kinetic energy (a) and temperature (b) obtained from the time spectral solver.

B. Perturbed Flow with Ablating Ramp

After obtaining the steady streaks in Section IV.A, the ramp is now numerically assumed to be made of solid camphor. Under these flow conditions, the solid camphor ramp undergoes ablation by sublimation reactions leading to blowing of camphor gas from the surface and the recession of the gas-solid interface. These interactions are handled by their respective methodologies for both INCA and CHAMPS as discussed in Section II.B. For the solid density of camphor, a value of 990 $\mathrm{kg\,m^{-3}}$ is taken [13], which dictates the recession speed of the solid according to Eq. 4. The recession speed acceleration factor discussed in Section II.B is set to 1×10^5 to obtain results within a reasonable number of computational hours. The results shown from both solvers consider the time instance when on average 0.1 mm of recession is observed.

The flow fields computed by INCA and CHAMPS are presented in Fig. 10. A slice in the spanwise plane at $z = 0.0$ m plots the Mach number and four slices in streamwise planes at $x = [0.021, 0.065, 0.085, 0.1]$ m are shown for the temperature distributions predicted by both solvers. Entrainment from the counter-rotating vortices of the steady streaks leads to the formation of alternating heating and cooling streaks on the surface along the spanwise direction. As anticipated from the higher mass blowing rates observed in Section III.C, the figure shows a slightly higher amplifications of the perturbation for INCA. These higher mass blowing rates can also be seen from the contours of camphor mass fractions shown in Fig. 11.

Effect of the heating streaks on the recession patterns over the surface of the ramp can be seen in Fig. 12. INCA predicts higher recession near the recirculation region, whereas CHAMPS predicts highest recession near reattachment point. Note that ablation is smoothly ramped up by a hyperbolic tangent function near the corner to avoid localizing the recession by preserving the mean ramp angle. Even though the streak amplitudes are higher for the INCA simulations, CHAMPS solution indicates a more distinct variation between the heating and the cooling streaks. This is suspected to be due to the additional energy balance employed in the material response boundary condition, which accounts for the variation of temperature along the wall. Overall, both solvers successfully predict the influence of the heating streaks on the recessing material surface.

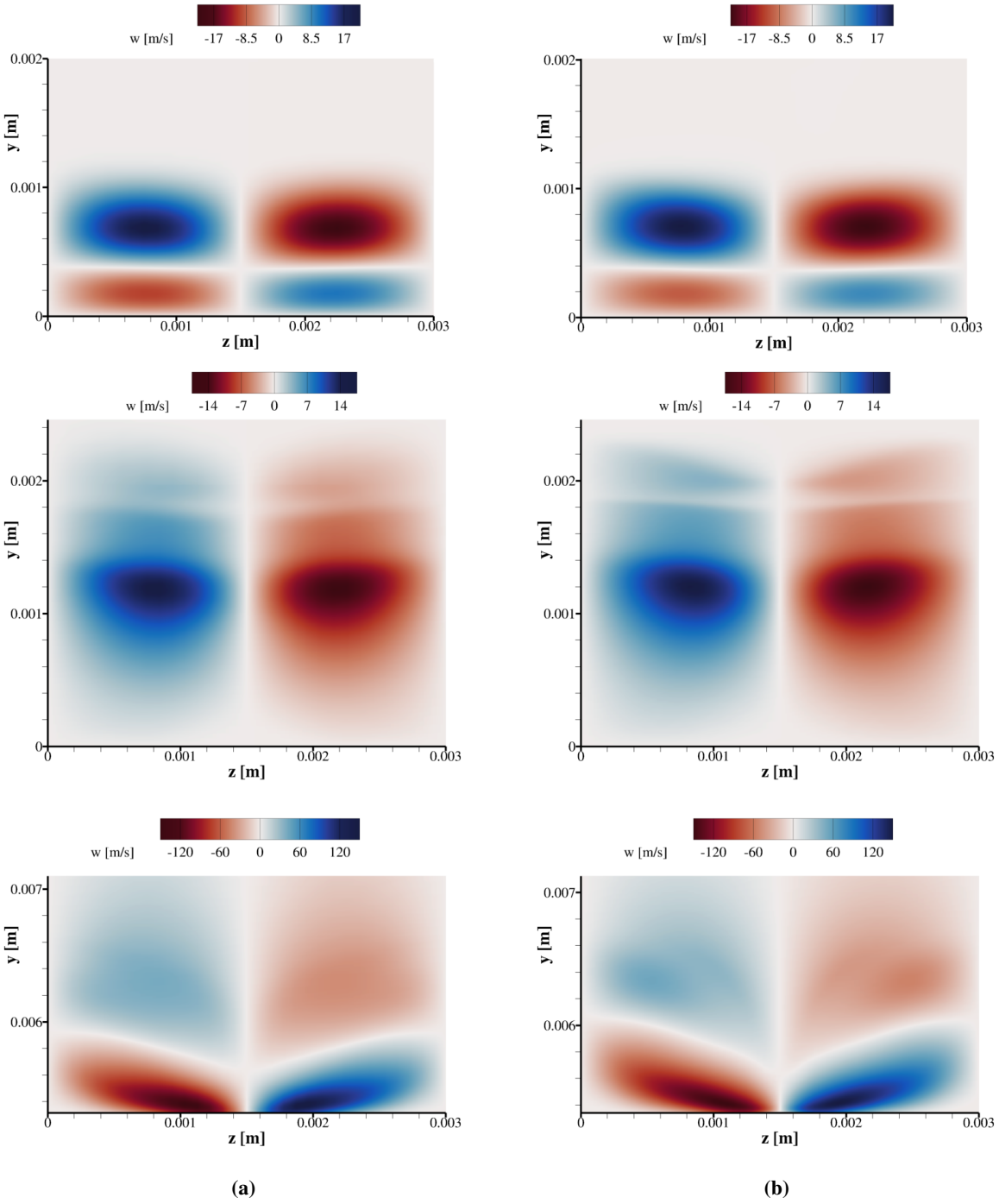

Fig. 9 Comparison of spanwise velocities at $x = 0.023$m (top) , $x = 0.030$m (middle), $x = 0.070$m (bottom) from INCA (left) and CHAMPS (right) for the 3-D compression ramp with steady streaks.

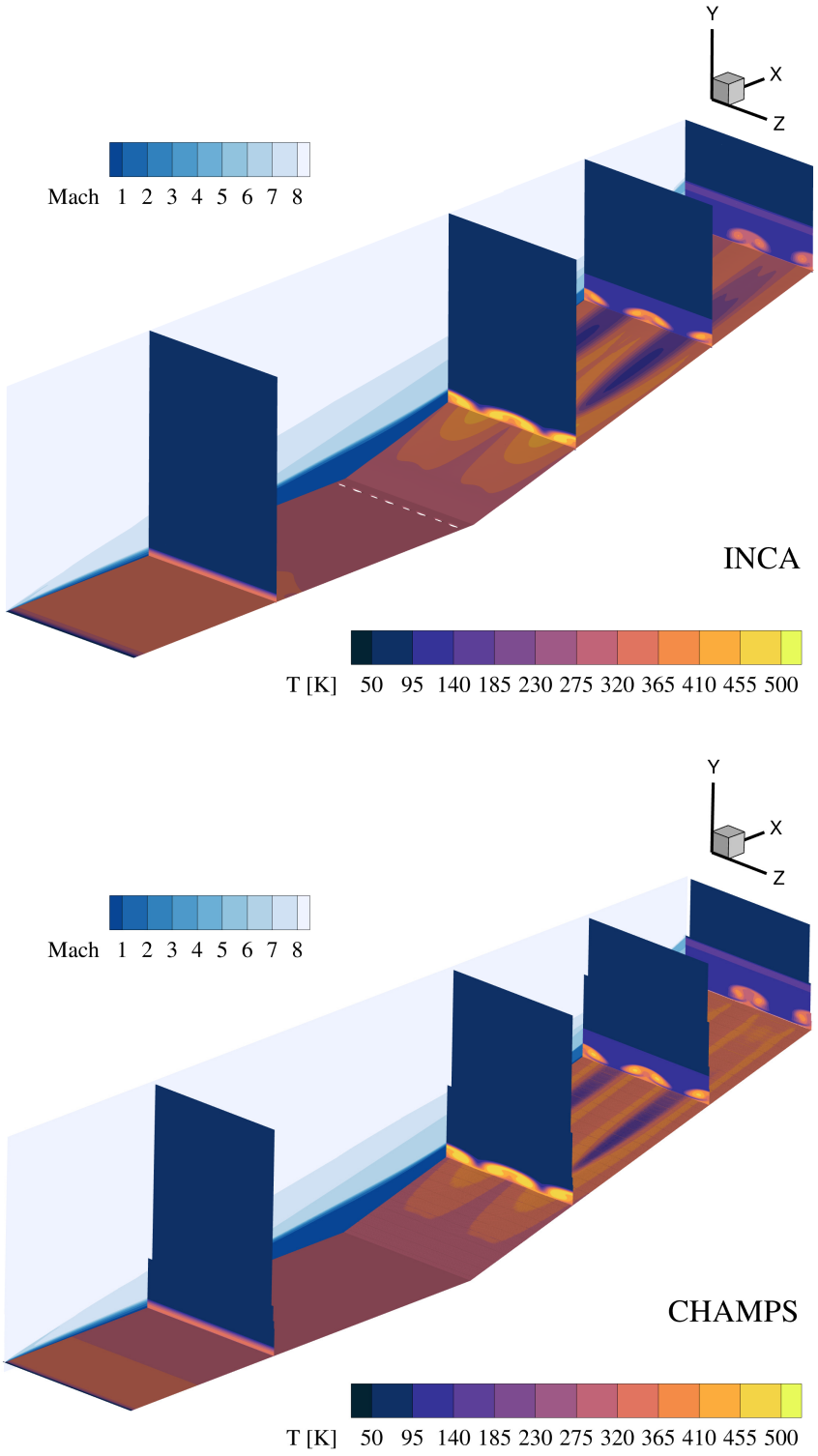

Fig. 10 Isometric views of INCA and CHAMPS solutions for the 3-D compression ramp with steady streaks and a camphor wall undergoing ablation. Background slice in the spanwise direction shows Mach number contours. Slices in the streamwise plane show temperature contours.

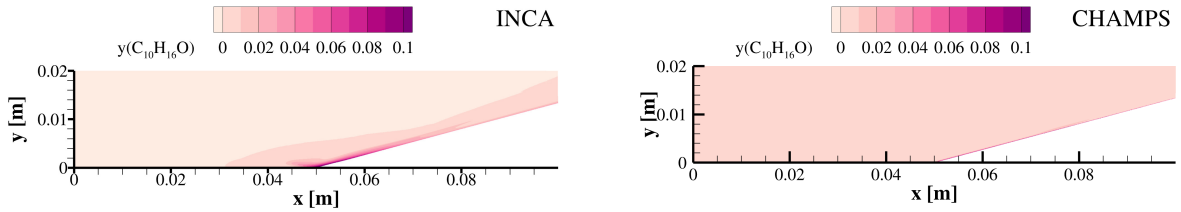

Fig. 11 Camphor mass fractions of INCA and CHAMPS solutions for the 3-D compression ramp with steady streaks and a camphor wall undergoing ablation.

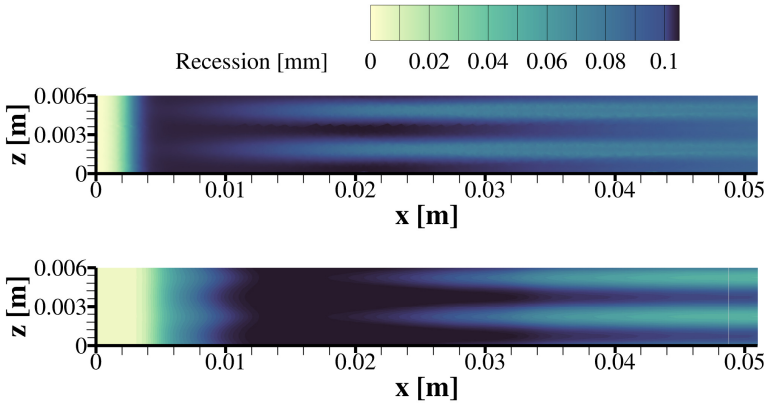

Fig. 12 Recession patterns of INCA (top) and CHAMPS (bottom) solutions for the 3-D compression ramp with steady streaks and a camphor wall undergoing ablation.

1. Transient Material Response

The spanwise gradients introduced by the primary streaks impose the heating streaks seen beginning near reattachment on the inclined ramp. It is therefore expected that this variation in input to the GSI and MR solvers would result in differential ablation on the ramp's surface. What is not so easily foreseen is the temporal evolution of this differential ablation. Figure 13 attempts to shed light on this by plotting the spanwise recession and heat flux distributions at $x = 0.065$ m from the compression ramp's leading edge. From the recession profiles shown in Fig 13a, one can see that at an early time instance in the simulation ($t_{MR} = 1$ seconds) the ablation is 2D dominated with minimal differential ablation. As time progresses, however, the differential ablation (peak to peak) becomes more and more pronounced. At the last time instance ($t_{MR} = 4$ seconds) the differential ablation is roughly 0.18 mm at $z = 2$ mm. This is interesting because just examining the heat flux (see Fig. 13b) at the same x location reveals a consistent decrease during the simulation. In light of this, one might expect the differential ablation to then subside. Figure 13c also demonstrates clearly, that the differential heat flux only decreases in magnitude until $t_{MR} = 4$ s. It appears then that the differential ablation is being amplified in time due to the heat flux spanwise distribution remaining in the same relative phase throughout the simulation. This allows the material in the same spanwise location (e.g., $z = 2.2$ mm) to consistently be ablated and results in the large valley of recession shown in Fig. 13a. The maximum in spanwise recession was then computed for each x location along the inclined ramp and plotted for several instances in time, as is shown in Figure 14a. This exhibits the localization of maximum recession to the reattachement region where heat flux is largest. Figure 14b then plots the maximum recession at $x = 0.07$ m as a function of time and displays the nearly constant ablation rate reached in the simulation.

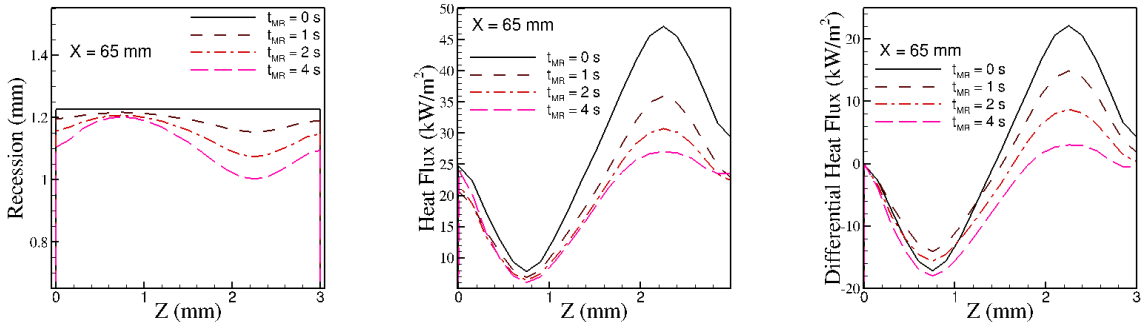

Fig. 13 Spanwise distribution at $x = 0.065$ m of recession (a), heat flux (b), and differential heat flux (c) for four instances in time.

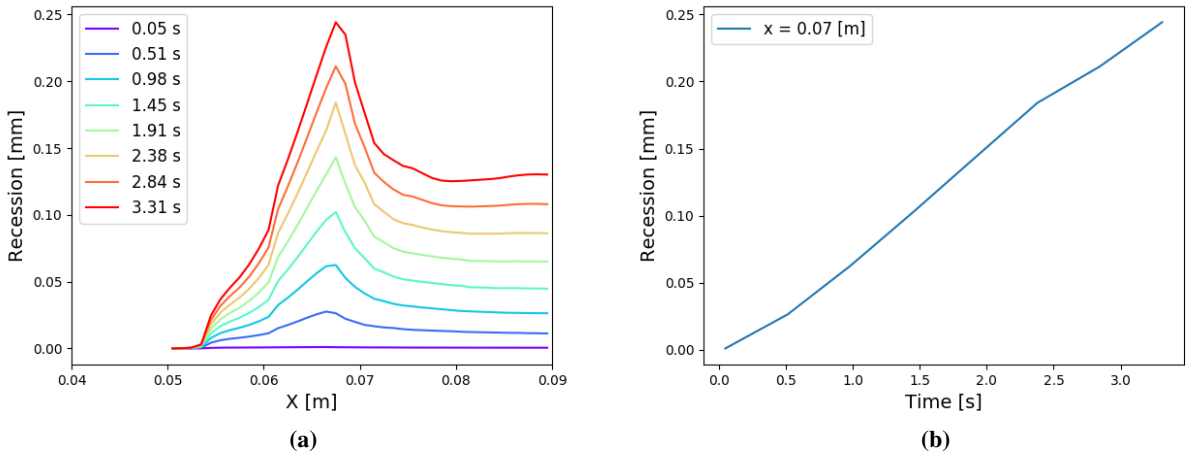

Fig. 14 Streamwise distribution of maximum (in span) recession on the compression ramp for several instances in time (a) and temporal evolution of said maximum for $x = 0.07$ m.

2. Influence of Ablation on Perturbation Growth

Influence of ablation on perturbation growth is quantified by comparing the results obtained with inert and ablative boundary conditions from the INCA solver. For these simulations, the domain length is extended to 0.2 m in the streamwise direction to investigate the onset of transition. The resulting flow fields from the same time instance are shown in Fig. 15. Slices in Fig. 10 are kept for the same values to mark the scale difference in the plots due to the extended domain. A careful eye would notice, the breakdown of the laminar flow occurs earlier for the ablative case. We observe a higher amplification rate under the influence of ablation. This is expected in the absence of complex gas-phase chemistry as in the current case. The major effect here is due to the blowing velocity from the surface, that amplifies the primary perturbation.

This finding is further supported by studying Fig. 16, where maximum spanwise speeds along streamwise locations are presented for the inert and ablative INCA solutions. These values are normalized with the amplitude at the initial perturbation location. The figure demonstrates that an amplification of 10 is reached immediately downstream of the impinging shock. Amplitudes for the inert and ablative cases mostly match until around 0.15 m; further downstream, a rapid amplification of the total perturbation is observed for the ablative case.

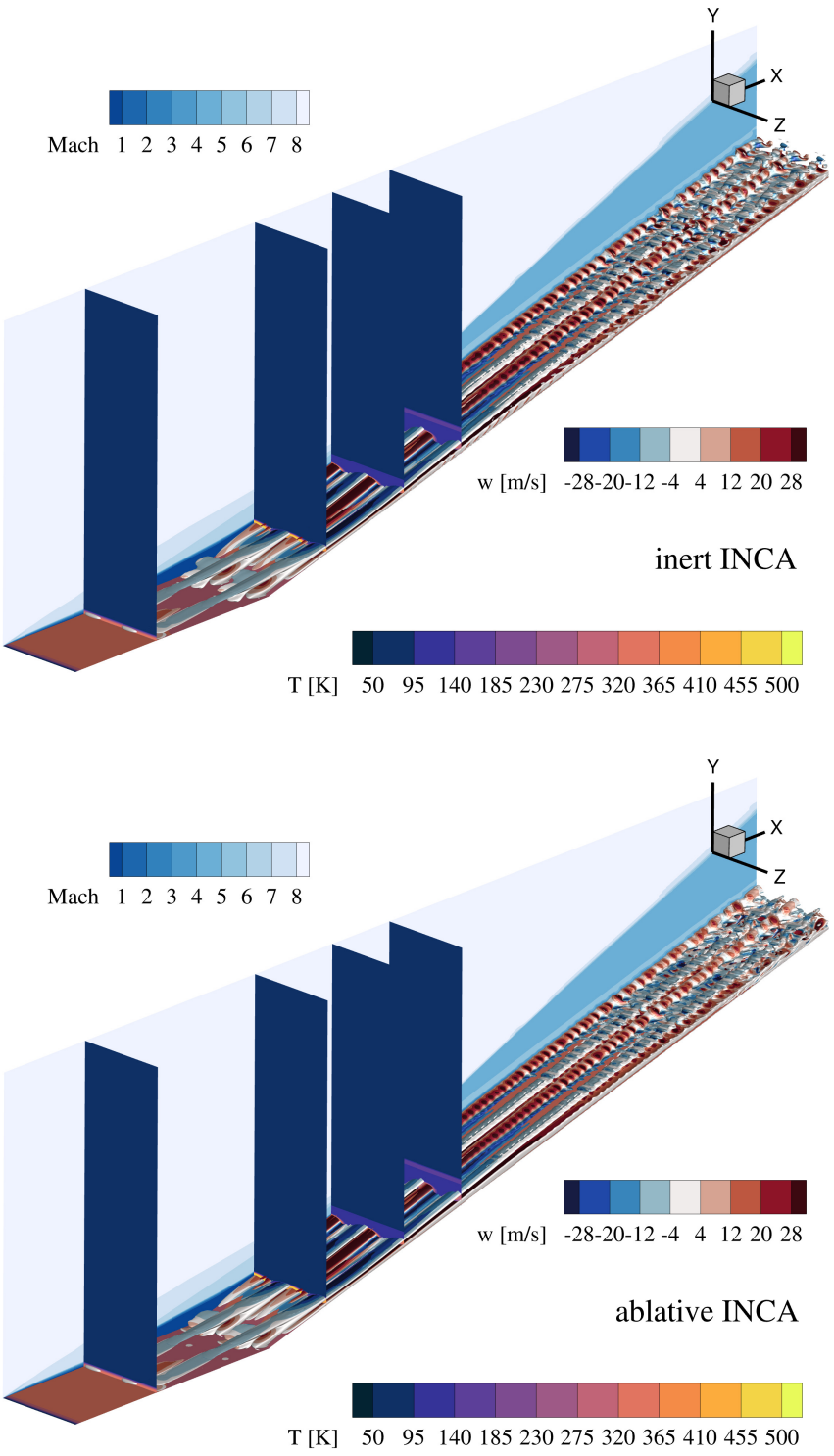

Fig. 15 Isometric views of inert and ablative INCA solutions for the 3-D compression ramp with steady streaks along the extended domain reaching to $0.2\,\mathrm{m}$ in the streamwise direction. Background slice in the spanwise direction shows Mach number contours. Slices in the streamwise plane show temperature contours and are kept in the plots to show the scale difference with respect to Fig. 10. Iso-surface of vorticity at $1 \times 10^4\,\mathrm{s}^{-1}$ is colored with the spanwise velocity.

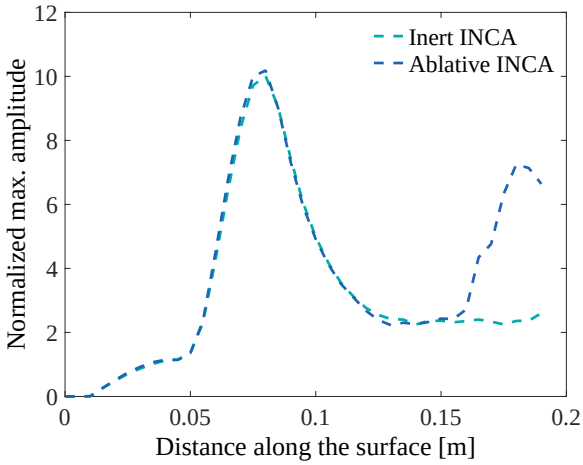

Fig. 16 Comparison of perturbation amplitudes for the inert and ablative INCA solutions for the 3-D compression ramp with steady streaks along the extended streamwise domain reaching to $0.2\,\mathrm{m}$ **in the streamwise direction.**

Additional calculations solving the nonlinear disturbance equations (NLDE) were performed on top of the smooth wall baseflow containing the converged steady streaks. The NLDE formulation in CHAMPS has been used for a variety of stability problems [57–59]. A pulse disturbance was introduced again to the domain, however, this time only 3 spanwise harmonics of the primary streak wavelength were introduced. The rationale here was that any secondary instability forming will derive energy from the primary streak and its gradients. Since strong spanwise gradients in flow variables are known to promote instability growth, and these gradients will possess similar spanwise periodicity of the primary streak, highly amplified disturbances riding spanwise gradients will most likely be higher spanwise harmonics. The result of this calculation is shown below in Fig. 17.

Here spanwise velocity perturbation iso-surfaces of (red/blue for ±0.001 m/s, respectively) are shown for three instances in time for the unsteady, pulse calculation to illustrate its temporal evolution. Also shown for reference are the baseflow iso-surfaces of zero streamwise velocity (white) and the heat flux at the surface of the ramp (blue and red). These features of the plot are meant to provide spatial context for the wavepacket, namely where they are relative to the reattachement line. The wavepacket farthest away, or on the left side of the ramp, is the first instance in time, and the wavepacket closest, or on the right side of the ramp, is the last instance in time. From the perspective view it is hard to discern the exact wavenumber dominating the wavepacket, however, at the first instance in time the wavepacket is clearly dominated by streaky structures similar to those instabilities supported by the streak-less baseflow. Then, at the second instance of time one can see the streak like structures being curled up by the primary streak as it lifts fluid away from the wall post reattachement. Finally, at the last instance in time the wavepacket has traveled inside the strongly amplified streaks long enough where a clear secondary instability has taken over. This is best recognized by the streamwise wavenumber now evident in the wavepacket towards its leading edge. The streamwise wavenumbers were seen to pop up in the longer domain results with INCA as well (see Fig. 15) prior to streak breakdown.

V. Conclusion

We have presented results from two independently developed solvers employing different numerical methods and fluid-ablation interaction modeling strategies for the case of a 15° compression ramp. The test case is first handled in 2-D for establishing the base flow and the fundamental flow feature agreements. Then, it is extended to 3-D to include perturbations in the flow leading to steady streaks comprising of streamwise counter rotating vortices. The rigid ramp is then replaced by solid camphor such that it ablates under these flow conditions and interacts with the perturbed flow through mass blowing, surface recession, and heat transfer. Our results show significant effects of fluid-ablation interactions on the perturbation growth and the eventual turbulent breakdown of the streak-vortex system. Both solvers provide qualitatively and quantitatively very similar results. The observed differences are in most instances due to different fluid-ablation interaction models, which lead to slightly different mass blowing rates. This work constitutes a first step towards predictive high-fidelity fluid-ablation interaction simulations.

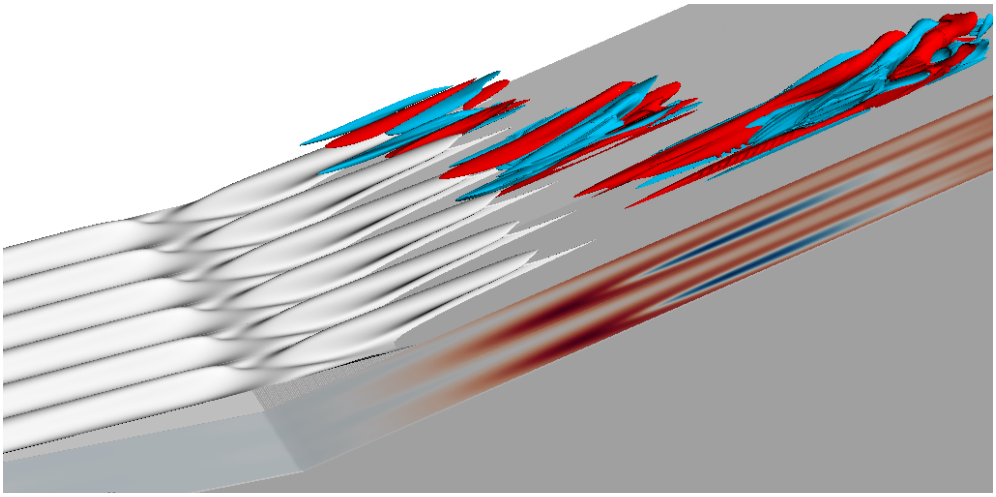

Fig. 17 Spanwise perturbation velocity iso-surfaces (± 0.001 m/s) for three instances in time (time increasing farthest to closest) shown in blue and red. Iso-surfaces of zero streamwise velocity for the baseflow included in white. Heat flux also shown to help illustrate the reattachment location.

Acknowledgements

Funding provided by NSF under CBET-2146100 with Dr. R. Joslin as program manager and the ACCESS program award no. 80NSSC21K1117 with Dr. Eric Stern as program manager are gratefully acknowledged. In addition, the majority of the simulations shown here from the University of Maryland were computed on facilities provided by the University of Maryland's High-Performance Computing Cluster (Zaratan). For simulations shown here from TU Delft, we thank the Delft High Performance Computing Centre for providing access to DelftBlue and the SURF Cooperative (www.surf.nl) for providing access to the National Supercomputer Snellius.

References

[1] Schneider, S. P., "Erratum on Laminar-Turbulent Transition on Reentry Capsules and Planetary Probes," *Journal of Spacecraft and Rockets*, Vol. 44, No. 2, 2007, pp. 464–484.

[2] Zhong, X., and Wang, X., "Direct numerical simulation on the receptivity, instability, and transition of hypersonic boundary layers," *Annual Review of Fluid Mechanics*, Vol. 44, 2012, pp. 527–561.

[3] Reed, H. L., Perez, E., Kuehl, J., Kocian, T., and Oliviero, N., "Verification and validation issues in hypersonic stability and transition prediction," *Journal of Spacecraft and Rockets*, Vol. 52, No. 1, 2015, pp. 29–37.

[4] Yang, H.-s., Liang, H., Guo, S.-g., Tang, M.-x., Zhang, C.-b., Wu, Y., and Li, Y.-h., "Research Progress of hypersonic boundary layer transition control experiments," *Advances in Aerodynamics*, Vol. 4, No. 1, 2022, pp. 1–54.

[5] Schneider, S. P., "Summary of hypersonic boundary-layer transition experiments on blunt bodies with roughness," *Journal of Spacecraft and Rockets*, Vol. 45, No. 6, 2008, pp. 1090–1105.

[6] Canning, T. N., Tauber, M. E., and Wilkins, M. E., "Review of recent ballistic range boundary-layer transition work on ablating bodies at Ames," *Boundary Layer Transition Specialists Study Group Meeting*, 1967.

[7] Schneider, S. P., "Hypersonic boundary-layer transition with ablation and blowing," *Journal of Spacecraft and Rockets*, Vol. 47, No. 2, 2010, pp. 225–237.

[8] Bellas Chatzigeorgis, G., Turchi, A., Viladegut, A., Chazot, O., Barbante, P. F., and Magin, T., "Development of catalytic and ablative gas-surface interaction models for the simulation of reacting gas mixtures," *23rd AIAA Computational Fluid Dynamics Conference*, 2017, p. 4499.

[9] Capriati, M., Prata, K., Schwartzentruber, T., Candler, G., and Magin, T., "Development of a nitridation gas-surface boundary condition for high-fidelity hypersonic simulations," *WCCM-ECCOMAS*, 2021.

[10] Needels, J. T., Duzel, U., Hanquist, K. M., and Alonso, J. J., "Sensitivity Analysis of Gas-Surface Modeling in Nonequilibrium Flows," *AIAA SCITECH 2022 Forum*, 2022, p. 1636.

[11] Chen, Y.-K., and Milos, F. S., "Multidimensional finite volume fully implicit ablation and thermal response code," *Journal of Spacecraft and Rockets*, Vol. 55, No. 4, 2018, pp. 914–927.

[12] Schroeder, O. M., Brock, J., Stern, E., and Candler, G. V., "A coupled ablation approach using Icarus and US3D," *AIAA SCITECH 2021 Forum*, 2021, p. 0924.

[13] Rotondi, M., Migliorino, M. T., Bianchi, D., Pagani, P., and Turchi, A., "Numerical Assessment of Camphor Ablation Flight Relevance in Hypersonic Wind-Tunnel Testing," *Journal of Spacecraft and Rockets*, 2022, pp. 1–18.

[14] Wheaton, B. M., Berridge, D. C., Wolf, T. D., Araya, D. B., Stevens, R. T., McGrath, B. E., Kemp, B. L., and Adamczak, D. W., "Final Design of the Boundary Layer Transition (BOLT) Flight Experiment," *Journal of Spacecraft and Rockets*, Vol. 58, No. 1, 2021, pp. 6–17.

[15] Araya, D., Bitter, N., Wheaton, B. M., Kamal, O., Colonius, T., Knutson, A., Johnson, H., Nichols, J., Candler, G. V., Russo, V., et al., "Assessment of Linear Methods for Analysis of Boundary Layer Instabilities on a Finned Cone at Mach 6," *AIAA AVIATION 2022 Forum*, 2022, p. 3247.

[16] Lugrin, M., Nicolas, F., Severac, N., Tobeli, J.-P., Beneddine, S., Garnier, E., Esquieu, S., and Bur, R., "Transitional shockwave/boundary layer interaction experiments in the R2Ch blowdown wind tunnel," *Experiments in Fluids*, Vol. 63, No. 2, 2022, pp. 1–19.

[17] He, S., and Zhong, X., "Hypersonic boundary-layer receptivity over a blunt cone to freestream pulse disturbances," *AIAA Journal*, Vol. 59, No. 9, 2021, pp. 3546–3565.

[18] Melander, L. J., Dwivedi, A., and Candler, G. V., "Numerical Investigation of Nosetip Bluntness Effects on Cone Frustum Boundary Layer Transition in Hypersonic Flow," *AIAA SCITECH 2022 Forum*, 2022, p. 0948.

[19] Gokcen, T., "On Characterization of Laminar to Turbulent Transitional Flow in the Truncated IHF Semi-Elliptical Nozzle," *AIAA AVIATION 2022 Forum*, 2022, p. 3504.

[20] Zhong, X., "A DNS Study on Hypersonic Boundary-Layer Receptivity and a New Transition Control Strategy by Surface Roughness," Tech. rep., Mechanical and Aerospace Engineering Department, University of California . . . , 2019.

[21] Saikia, B., and Brehm, C., "Effect of Distributed Surface Roughness on the Stability of High-Speed Flows." *AIAA SCITECH 2022 Forum*, 2022, p. 1212.

[22] Egorov, I., Obraz, A., Palchekovskaya, N., and Fedorov, A., "Numerical Simulation of Gas Injection Effect on Boundary Layer Instability for Space Vehicles," *IUTAM Laminar-Turbulent Transition*, Springer, 2022, pp. 107–115.

[23] Kerth, P., Wylie, S., Ravichandran, R., and McGilvray, M., "Gas Injection into Second Mode Instability on a 7 degree Cone at Mach 7," *AIAA AVIATION 2022 Forum*, 2022, p. 3856.

[24] Mortensen, C. H., and Zhong, X., "Real-Gas and Surface-Ablation Effects on Hypersonic Boundary-Layer Instability over a Blunt Cone," *AIAA Journal*, Vol. 54, No. 3, 2016, pp. 980–998. https://doi.org/10.2514/1.J054404.

[25] Mortensen, C. H., and Zhong, X., "Real-gas and surface-ablation effects on hypersonic boundary-layer instability over a blunt cone," *AIAA Journal*, Vol. 54, No. 3, 2016, pp. 980–998.

[26] Miró Miró, F., and Pinna, F., "Decoupling ablation effects on boundary-layer stability and transition," *Journal of Fluid Mechanics*, Vol. 907, 2021.

[27] Karimi, M., and Stemmer, C., "Direct Numerical Simulation of the chemically reacting boundary layer of hypersonic flows subject to ablation Machine," *2nd International Conference on Flight Vehicles, Aerothermodynamics and Re-entry Missions & Engineering (FAR)*, 2022.

[28] Rogers, R. E., Schroeder, O. M., Melander, L. J., and Candler, G. V., "Analysis of Ablation on Boundary Layer Stability of the Reentry F Flight Vehicle," *AIAA AVIATION 2022 Forum*, 2022, p. 3775.

[29] Passiatore, D., Sciacovelli, L., Cinnella, P., and Pascazio, G., "Finite-rate chemistry effects in turbulent hypersonic boundary layers: A direct numerical simulation study," *Physical Review Fluids*, Vol. 6, No. 5, 2021, p. 054604.

[30] Urzay, J., and Di Renzo, M., "Engineering aspects of hypersonic turbulent flows at suborbital enthalpies," *Annual Research Briefs, Center for Turbulence Research*, 2021, pp. 7–32.

[31] Trevino, L., "Numerical Simulation of Surface Patterns on Sublimating Ablative Materials," Ph.D. thesis, 2021.

[32] Patel, M., "Hypersonic flows around complex geometries with adaptive mesh refinement and immersed boundary method," 2023.

[33] Trevino, L., "Numerical Simulation of Surface Patterns on Sublimating Ablative Materials," Ph.D. thesis, University of Minnesota, Minneapolis, Minnesota, 05 2021.

[34] Candler, G. V., Johnson, H. B., Nompelis, I., Gidzak, V. M., Subbareddy, P. K., and Barnhardt, M., *Development of the US3D Code for Advanced Compressible and Reacting Flow Simulations*, 2015. https://doi.org/10.2514/6.2015-1893.

[35] Patel, M., "Hypersonic flows around complex geometries with adaptive mesh refinement and immersed boundary method," Ph.D. thesis, Imperial College London, London, United Kingdom, 03 2023.

[36] Dungan, S. D., McQuaid, J. A., Zibitsker, A. L., Martin, A., and Brehm, C., *Numerical Investigation of Fluid-Ablation Interactions for a Mach 5.3 Transitional Boundary Layer Flow Over a 13 Degree Cone*, 2023. https://doi.org/10.2514/6.2023-0476.

[37] Chuvakhov, P. V., Borovoy, V. Y., Egorov, I. V., Radchenko, V. N., Olivier, H., and Roghelia, A., "Effect of Small Bluntness on Formation of Görtler Vortices in a Supersonic Compression Corner Flow," *Journal of Applied Mechanics and Technical Physics*, Vol. 58, 2017, pp. 975–989. https://doi.org/10.1134/S0021894417060037.

[38] Dwivedi, A., Sidharth, G. S., Nichols, J. W., Candler, G. V., and Jovanović, M. R., "Reattachment streaks in hypersonic compression ramp flow: An input-output analysis," *Journal of Fluid Mechanics*, 2019, pp. 113–135. https://doi.org/10.1017/jfm.2019.702.

[39] Zibitsker, A. L., McQuaid, J. A., Brehm, C., and Martin, A., "Validation and analysis of a coupled fluid-ablation framework for modeling low-temperature ablator," *International Journal of Heat and Mass Transfer*, Vol. 218, 2024, p. 124728.

[40] Hickel, S., Egerer, C. P., and Larsson, J., "Subgrid-scale modeling for implicit large eddy simulation of compressible flows and shock-turbulence interaction," *Physics of Fluids*, Vol. 26, No. 10, 2014, p. 106101.

[41] Müller, H., Niedermeier, C. A., Matheis, J., Pfitzner, M., and Hickel, S., "Large-eddy simulation of nitrogen injection at trans-and supercritical conditions," *Physics of Fluids*, Vol. 28, No. 1, 2016, p. 015102.

[42] Jiang, G.-S., and Shu, C.-W., "Efficient implementation of weighted ENO schemes," *Journal of Computational Physics*, Vol. 126, No. 1, 1996, pp. 202–228.

[43] Toro, E. F., *Riemann solvers and numerical methods for fluid dynamics: a practical introduction*, Springer-Verlag, Berlin, 2013.

[44] Gottlieb, S., and Shu, C.-W., "Total variation diminishing Runge-Kutta schemes," *Mathematics of Computation*, Vol. 67, No. 221, 1998, pp. 73–85.

[45] Örley, F., Pasquariello, V., Hickel, S., and Adams, N. A., "Cut-element based immersed boundary method for moving geometries in compressible liquid flows with cavitation," *Journal of Computational Physics*, Vol. 283, 2015, pp. 1–22.

[46] Baskaya, A., and Hickel, S., "An Accurate Reconstruction and Interpolation Scheme for a Conservative Cut-Cell Immersed Boundary Method with Gas-Surface Interactions," *14th International ERCOFTAC Symposium on Engineering Turbulence Modelling and Measurements (ETMM14)*, 2023.

[47] Başkaya, A. O., Capriati, M., Turchi, A., Magin, T., and Hickel, S., "Assessment of Immersed Boundary Methods for Hypersonic Flows with Gas-Surface Interactions," *Computers & Fluids*, Vol. 270, 2024, p. 106134. https://doi.org/10.1016/j.compfluid.2023.106134.

[48] Brehm, C., Barad, M., Housman, J., and Kiris, C., "A comparison of higher-order finite-difference shock capturing schemes," *Computers & Fluids*, Vol. 122, 2015, pp. 184 – 208. https://doi.org/https://doi.org/10.1016/j.compfluid.2015.08.023.

[49] Brehm, C., Hader, C., and Fasel, H., "A locally stabilized immersed boundary method for the compressible Navier–Stokes equations," *Journal of Computational Physics*, Vol. 295, 2015, pp. 475–504. https://doi.org/10.1016/j.jcp.2015.04.023.

[50] Scoggins, J. B., Leroy, V., Bellas-Chatzigeorgis, G., Dias, B., and Magin, T. E., "Mutation++: Multicomponent thermodynamic and transport properties for ionized gases in c++," *SoftwareX*, Vol. 12, 2020, p. 100575.

[51] Zibitsker, A. L., McQuaid, J. A., Brehm, C., and Martin, A., "Validation and analysis of a coupled fluid-ablation framework for modeling low-temperature ablator," *International Journal of Heat and Mass Transfer*, Vol. 218, 2024. https://doi.org/10.1016/j.ijheatmasstransfer.2023.124728.

[52] McQuaid, J. A., Zibitsker, A., Martin, A., and Brehm, C., "An Immersed Boundary Method for Hypersonic Viscous Flows," *AIAA Science and Technology Forum and Exposition Forum*, Virtual Event, 2021, pp. 1–16. https://doi.org/10.2514/6.2021-0926.

[53] McQuaid, J., Zibitsker, A., Martin, A., and Brehm, C., "Heat Flux Predictions for High Speed Flows with an Immersed Boundary Method," *AIAA Aviation Forum*, American Institute of Aeronautics and Astronautics, 2021. https://doi.org/10.2514/6.2021-3145.

[54] Zibitsker, A. L., McQuaid, J., Brehm, C., and Martin, A., "Fully-Coupled Simulation of Low Temperature Ablator and Hypersonic Flow Solver," *AIAA SCITECH 2022 Forum*, 2022, p. 0676. https://doi.org/https://doi.org/10.2514/6.2022-0676.

[55] Zibitsker, A. L., McQuaid, J. A., Brehm, C., and Martin, A., *Study of a Two-Dimensional Shape Change of Blunt-Body Geometries at Hypersonic Conditions Using Fully Coupled Simulation*, 2022. https://doi.org/10.2514/6.2022-4006.

[56] Haas, A. P., Browne, O. M. F., Fasel, H., and Brehm, C., "A time-spectral approximate Jacobian based linearized compressible Navier-Stokes solver for high-speed boundary-layer receptivity and stability," *Journal of Computational Physics*, Vol. 405, 2020.

[57] Browne, O. M. F., Haas, A. P., Fasel, H. F., and Brehm, C., "A nonlinear compressible flow disturbance formulation for adaptive mesh refinement wavepacket tracking in hypersonic boundary-layer flows," *Computers and Fluids*, Vol. 240, 2022, p. 105395. https://doi.org/10.1016/j.compfluid.2022.105395.

[58] Browne, O. M. F., Hasnine, S. M. A. A., and Brehm, C., "Numerical Method for Particulate-Induced High-Speed Boundary-Layer Transition Simulation," *AIAA*, Vol. 59, No. 4, 2021, pp. 1196–1213. https://doi.org/10.2514/1.J059544.

[59] Araya, D. B., Bitter, N. P., Wheaton, B. M., Kamal, O., Colonius, T., Knutson, A. L., Johnson, H. B., Nichols, J. W., Candler, G. V., Russo, V., and Brehm, C., "Linear Analysis of Boundary-Layer Instabilities on a Finned-Cone at Mach 6," *AIAA Journal, under review*, 2023. https://doi.org/10.48550/arXiv.2303.10747.